Journal of Superconductivity and Novel Magnetism (2026) 39:42
https://doi.org/10.1007/s10948-026-07144-5

RESEARCH

Structural and Magnetic Characteristics of $CoFe_xNi_{2-x}S_4$ ($x \leq 0.06$) Nanothiospinels: DFT Calculations

S. Caliskan[1] · M. A. Almessiere[2,3] · A. Baykal[4,5] · Y. Slimani[2] · A. Mihmanlı[6] · S. E. Shirsath[7] · L. I. Al-Jumaiah[2]

Received: 10 March 2025 / Accepted: 4 February 2026 / Published online: 16 February 2026

Abstract
Microspheres of $CoFe_xNi_{2-x}S_4$ ($x \leq 0.06$) nanothiospinels (NTSs) were successfully synthesized hydrothermally. The influence of Fe^{3+} ion substitution on the morphology, structure, and magnetic performance of the products is carefully investigated. Magnetic properties of $CoFe_xNi_{2-x}S_4$ ($x \leq 0.06$) NTSs are analyzed at 300 K (RT) and 10 K between ±50 kOe. At both temperatures, ferromagnetic nature (and hysteresis loops) is not detected for samples with $x < 0.03$. For the host sample ($x = 0.00$), while a diamagnetic behavior was observed at 300 K, paramagnetic behavior was exhibited at 10 K. Kinks, showing up in the hysteresis loops at 10 K, disappear at 300 K. The coercivity values of Fe-doped NTSs ($0.03 \leq x \leq 0.06$) at both at RT and 10 K demonstrate their magnetically hard nature. These results highlight that the Ni dopants can be harnessed to achieve desired magnetic properties of $CoFe_xNi_{2-x}S_4$ NTSs. The obtained findings show the potential for tuning the magnetic properties of $CoFe_xNi_{2-x}S_4$ nanothiospinels, making them promising candidates for use in spintronics, magnetic data storage, and sensors.

Keywords CoNi nanothiospinels · Hydrothermal synthesis · Microstructure · Magnetic properties · DFT study

1 Introduction

Metal sulfide nanoparticles demonstrate substantial improvements in surface shape, electrical conductivity, thermal stability, varied redox characteristics, and exceptional durability, resulting in effective applications for energy conversion, storage, and environmental remediation. Recently, spinel sulphides (especially Co-Ni sulphides, NCS) received the attention of material scientists due to their use in different applications such as microwave high-frequency sensors, platinum-free counter electrode for dye-sensitized solar cells, recording device, electrocatalytic energy conversion, storage devices, magnetic resonators supercapacitors, high-density electronic mass storage appliance, organophosphate pesticide biosensors, lithium-ion batteries, supercapacitors, and bifunctional electrocatalyst for oxygen reduction or evolution reactions [1–3].

Spinel metallic sulphides (e.g., $NiCo_2S_4$) are also important material in oxygen electrocatalysis due to their electronic conductivity, favourable electronic structure, multivalent oxidation state, good mechanical and thermal stability, etc [4, 5]. The replacement of O with S may generate a more flexible structure with the elongation of chemical bonds hence this makes the structure easier for electrons to

✉ A. Baykal
abdulhadibaykal@aydin.edu.tr

1 Department of Mathematical, Applied, and Physical Sciences, University of Houston-Clear Lake, Houston, TX 77058, USA

2 Department of Biophysics, Institute for Research and Medical Consultations (IRMC), Imam Abdulrahman Bin Faisal University, P.O. Box 1982, Dammam 31441, Saudi Arabia

3 Department of Physics, College of Science, Imam Abdulrahman Bin Faisal University, P.O. Box 1982, Dammam 31441, Saudi Arabia

4 Food Engineering Department, Faculty of Engineering, Istanbul Aydin University, Istanbul 34295, Türkiye

5 Basic Pharmacy Department, Pharmacy Faculty, Istanbul Aydin University, Istanbul 34295, Türkiye

6 Faculty of Dentistry, Gelişim University, Avcılar-Istanbul 34310, Türkiye

7 School of Materials Science and Engineering, University of New South Wales (UNSW), Kensington-Sydney 2052, Australia

be transported in this tuned structure, which can enhance the electrochemical performances of supercapacitors [6]. The electrical conductivity of is about 100 times that of $NiCo_2O_4$ [6, 7]. Beknalkar et al. [8] studied the charge storage dynamics and super capacitive features of hydrothermally synthesized $MnCo_2S_4$. Song et al. [2] used $CoNi_2S_4$ for organic dye degradation. Liu et al. [9] fabricated the Ni-Co sulfide heterostructures with enhanced electrochemical performance and stable thermodynamic interfaces. Li et al. [10] used the spinel-type bimetal sulfides for lithium-sulfur batteries.

The synthesis, characterization, investigation of magnetic characteristics, and DFT study of hydrothermally synthesized $CoFe_xNi_{2-x}S_4$ ($x \leq 0.06$) NTSs have been presented for the first time in this study. The magnetic characteristics of spinel compounds highly depend on the electronic configurations and occupancy of the cations at their tetrahedral (T_d) and octahedral (O_h) sites. In the proposed $CoFe_xNi_{2-x}S_4$ nanothiospinel system, replacing some Ni^{2+} ions with Fe^{3+} ions can be a thoughtful approach to tune the electronic and magnetic behaviors of the material. Indeed, this is driven by the distinct electronic configurations of Ni^{2+} and Fe^{3+} ions; Ni^{2+} ion: $[Ar]3d^8$, possessing two unpaired electrons, and Fe^{3+} ion: $[Ar]3d^5$, possessing five unpaired electrons. Accordingly, we are inserting ions with a significantly higher number of unpaired electrons into the crystal lattice by substituting Ni^{2+} with Fe^{3+} ions. One would expect to increase the net magnetic moment of the overall system and reinforce the super-exchange interactions between different cations, eventually serving as the driving force for the observed transition from a non-magnetic state to a ferromagnetic one. The present work investigates this specific substitution mechanism to demonstrate its effectiveness in controlling the magnetic properties of the $CoFe_xNi_{2-x}S_4$ system.

2 Experimental

2.1 Chemicals

The $CoFe_xNi_{2-x}S_4$ ($x \leq 0.06$) NTSs have been fabricated via a one-step hydrothermal route. The high purity of $Co(NO_3)_2{\cdot}6H_2O$, $Fe(NO_3)_3{\cdot}6H_2O$, $Ni(NO_3)_2{\cdot}6H_2O$, and thiourea (CH_4N_2S) were received from Merck. Nickel foam (cleaning through ultrasonication in ethanol-deionized water (DI) solution followed by drying with N_2 gas) was employed as both the deposition substrate.

2.2 Synthesis and Characterization

The chemicals employed are of analytical grades and used without any further purification. The stoichiometric amount of metal nitrates and thiourea were dissolved in 50 mL of DI water via stirring. 2 ml of Ethylene diamine was added to the mixture and sonicated for 1 h. Afterward, the solution was transferred to the 100 mL Stainless-steel autoclave (Teflon lined). The sealed Teflon-lined autoclave was heated at 200 °C for 12 h. After the hydrothermal reaction and cooling steps, solid product of $CoNi_2S_4$ NTSs washed with DI H_2O, and ethanol then dried at 80 °C for overnight. The same hydrothermal procedure was repeated for other "*x*" ratios [11].

The crystal structure was validated by an X-ray diffractometer (Rigaku Benchtop Miniflex, Cu Kα radiation) in range $2\Theta = 20–70^{o}$. The surface analysis of the products was completed by scanning electron microscopy (SEM, FEI), energy dispersive X-ray spectroscopy (EDX, AMETEK attached to Tescan Vega 3 SEM), and transmission electron microscopy (TEM, JEOL). The magnetic properties of products were investigated by Quantum Design PPMS DynaCool-9 coupled with a VSM head. Additionally, density functional theory (DFT) calculations were conducted to complement the experimental results and provide atomistic-level exploration of their structural and electronic characteristics.

3 Results & Discussion

3.1 Structure and Morphology

The unit cell diagram and investigation of $CoFe_xNi_{2-x}S_4$ ($x \leq 0.06$) NTSs crystal structure was proceed by the XRD powder patterns were represented in Fig. 1**(a and b)**. All samples displayed a mix phase of cubic $CoNi_2S_4$ siegenite (space group *Fd*−3*m*) phase and cubic CoS_2 (space group *Pa*−3**)** phase in all compositions and becomes more distinct at $x = 0.06$ [12, 13]. The intensity of second phase CoS_2 increases with increasing the ratio of Fe due to disturbing the lattice by varying in cation distribution [14]. The lattice parameters were estimated through Match3! and Full-proof software. The crystallite sizes of samples were calculated by the well-known Scherrer equation as displayed in Table 1. The lattice parameter was found to slightly increase with the rising ratio of Fe^{3+} in samples due to an expansion in the lattice as a result of difference in ionic radii between Fe and Ni [15]. We can state that iron is successfully inserted into the lattice structure of cubic $CoNi_2S_4$ siegenite. The crystallite size (D_{XRD}) ranges between 23 and 42 nm. W–H method has been utilized the XRD patterns to calculate the micro strain (ε) of $CoFe_xNi_{2-x}S_4$ ($x \leq 0.06$) NTSs was presented in Fig. 2 and listed in Table 1. In this method, the microstrain presented positive values shows a tensile stress, where the crystal lattice is expanded [16].

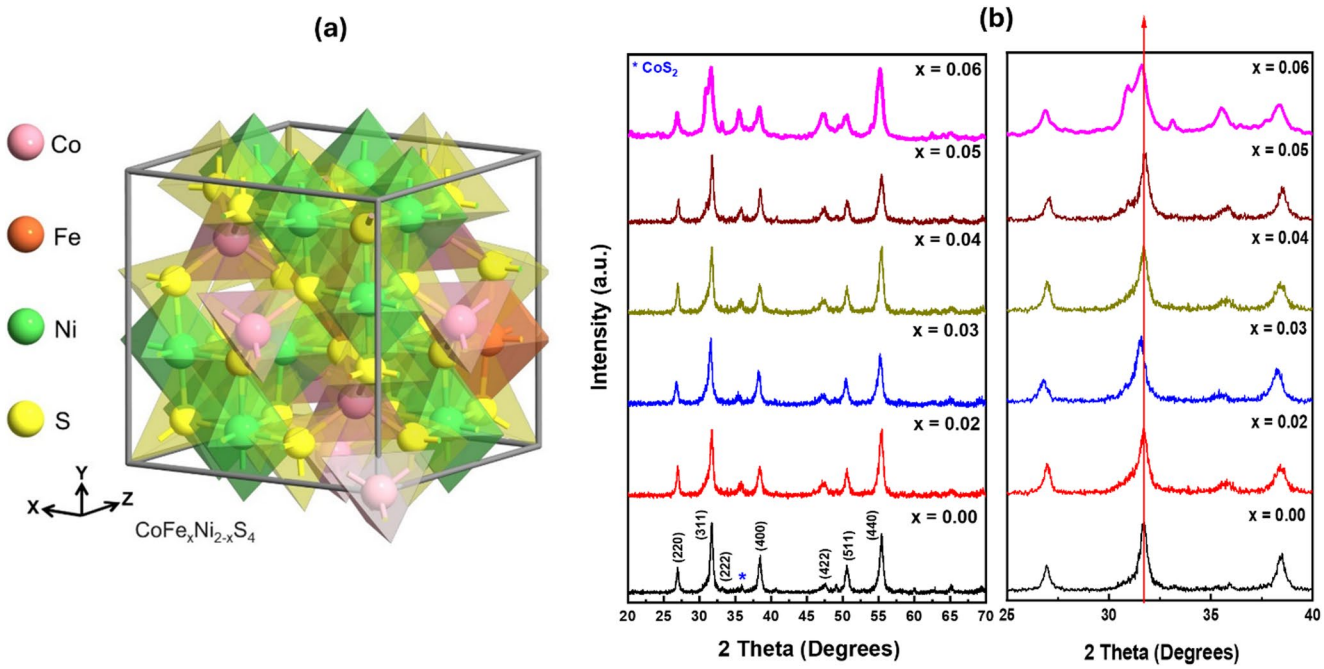

Fig. 1 **(a)** Unit cell representation and **(b)** XRD powder patterns of $CoFe_xNi_{2-x}S_4$ ($x \leq 0.06$) NTSs

Table 1 Structural parameters of $CoFe_xNi_{2-x}S_4$ ($x \leq 0.06$) NTSs

x	a_0 (Å)	D_{XRD} (nm)	MW (g/mol)	Micro strain (ε) W-H x10^{-3} (lines-2 m^{-4})	d_x (g/cm^3)	V (Å^3)	L(A) (nm)	L(B) (nm)
0.00	9.3996	42.3	298.850	**3.5**	4.815	824.820	4.061	3.316
0.02	9.4096	35.9	298.907	**3.6**	4.816	824.820	4.061	3.316
0.03	9.4045	19.6	298.936	**4**	4.785	830.291	4.070	3.323
0.04	9.4007	33.4	298.964	**2.9**	4.836	821.567	4.056	3.311
0.05	9.4072	24.3	298.993	**2.4**	4.779	831.392	4.072	3.324
0.06	9.4201	23.9	299.021	**2.8**	4.780	831.392	4.072	3.324

Figure 3 presents the SEM images of $CoFe_xNi_{2-x}S_4$ ($x \leq 0.06$) NTSs which illustrates the agglomeration of microsphere wool ball particles of varying size, with a size range less than 1 µm. In addition, the inside hollow structure of the spherical wool-ball shape [17–19] was demonstrated in the ratios $x = 0.02$, 0.03, and 0.04. The observed reduction in grain size with Fe doping is most likely caused by the introduction of lattice strain, which affects and hinders the crystal growth. However, a degree of aggregation is shown to a certain extent, which is occurred as a result of the high surface energy of the particles [20]. The energy-dispersive analysis (EDX) and elemental mapping demonstrate the successful synthesis of $CoNi_2S_4$, as evidenced by the presentation of Co, Ni, S and Fe in Fig. 4. The TEM and HR-TEM analyses were conducted to further characterize the microstructures of $CoFe_xNi_{2-x}S_4$ ($x \leq 0.06$) NTSs, as illustrated in Fig. 5. The TEM image displays a concentrated concentration of spherical particles. Crystal planes such as (444), (400), (333), and (331) were identified by the calculation of the distance between the lattice fringes using the HR-TEM image, which are pertinent to the cubic siegenite phase.

3.2 Cation Distribution

The Bertaut method was applied for the cation distribution of $CoFe_xNi_{2-x}S_4$ ($x \leq 0.06$) NTSs based on XRD patterns [21]. Table 2 presents the cation distribution in the $CoFe_xNi_{2-x}S_4$ ($x \leq 0.06$) NTSs, illustrating how cations (Co^{2+}, Ni^{2+}, Fe^{3+}) are allocated between the A-site and B-site of the spinel structure as the composition varies with x. It should be noted that S ions are not considered in the cation distribution. For the initial composition ($x = 0.0$), the A-site is predominantly occupied by nickel ions (Ni^{2+}) with a small amount of cobalt (Co^{2+}), while the B-site has a higher concentration of cobalt compared to iron. As iron (Fe^{3+}) is introduced into the system at $x = 0.02$, Fe^{3+} begins to occupy the B-site, replacing a small fraction of Ni, while the A-site composition remains unchanged. With $x = 0.03$, the amount of Fe in the B-site increases slightly, further replacing Ni, and the A-site remains stable with the same cation distribution as in the previous compositions. At $x = 0.04$, the Fe^{3+} ion concentration in the B-site continues to increase, replacing more Ni, while the A-site still remains unaffected by the

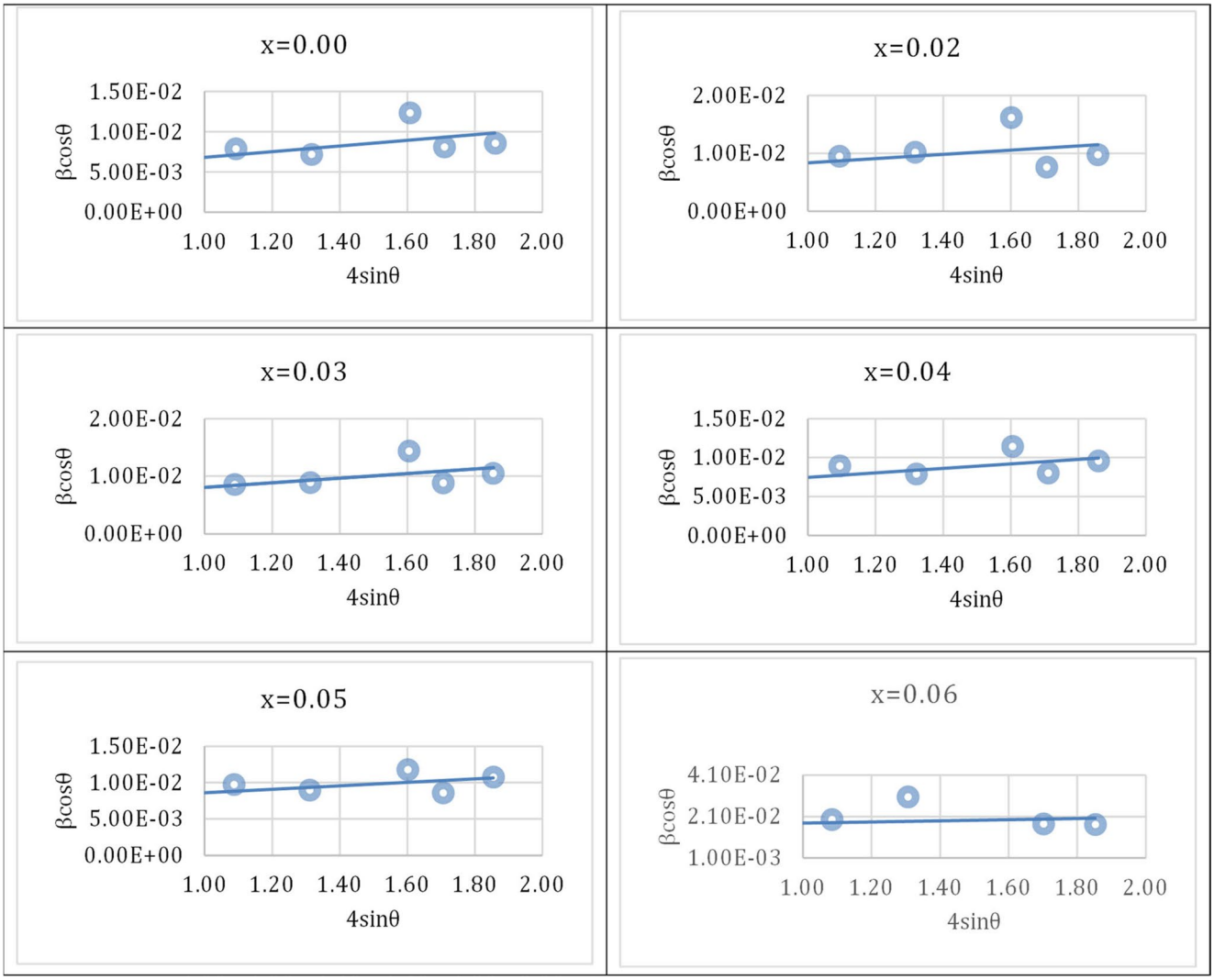

Fig. 2 Williamson–Hall plots of $CoFe_xNi_{2-x}S_4$ ($x \leq 0.06$) NTSs

addition of Fe^{3+}. For $x = 0.05$, Fe^{3+} in the B-site increases to 0.05, indicating a gradual substitution of Ni^{2+} with Fe^{3+}, while the A-site composition remains consistent with earlier compositions. At $x = 0.06$, Fe^{3+} occupies 0.06 of the B-site, showing a continuous trend of Fe^{3+} replacing Ni^{2+} in the B-site, with the A-site remaining unchanged throughout the compositions. Generally, in the inverse spinel structure, Fe^{3+} and Co^{2+} are expected to occupy the octahedral B-site according to the single-ion model [22, 23].

Observations and trends indicate that the A-site composition ($Co_{0.15}Ni_{0.85}$) remains constant across all compositions ($x=0.0$ to $x=0.06$), suggesting that the introduction of Fe^{3+} does not affect the cation distribution in the A-site. In contrast, the B-site shows a progressive substitution of Ni^{2+} by Fe^{3+} as the value of x increases, indicating that Fe^{3+} preferentially occupies the B-site over the A-site in the spinel structure. The amount of cobalt in both the A-site and B-site remains consistent throughout the compositions, implying that cobalt's distribution is not influenced by the varying Fe^{3+} concentration. The decrease in Ni^{2+} content in the B-site with increasing x indicates that Ni is being systematically replaced by Fe^{3+}, reflected in the gradual increase of Fe^{3+} and corresponding decrease of Ni^{2+} in the B-site. In conclusion, the cation distribution in the $CoFe_xNi_{2-x}S_4$ NTSs shows a clear preference for Fe^{3+} to occupy the B-site, while the A-site composition remains unaffected by the introduction of Fe^{3+}. This consistent pattern of Fe^{3+} substitution in the B-site, while maintaining stable Co^{2+} and Ni^{2+} levels in the A-site, indicates specific site preferences and stability within the spinel structure of this system.

3.3 Magnetic Traits

The magnetic traits of $CoFe_xNi_{2-x}S_4$ ($x \leq 0.06$) NTSs were analyzed at RT (room temperature) and 10 K under ±50 kOe. Figure 6 provides the relevant *M(H)* curves at each

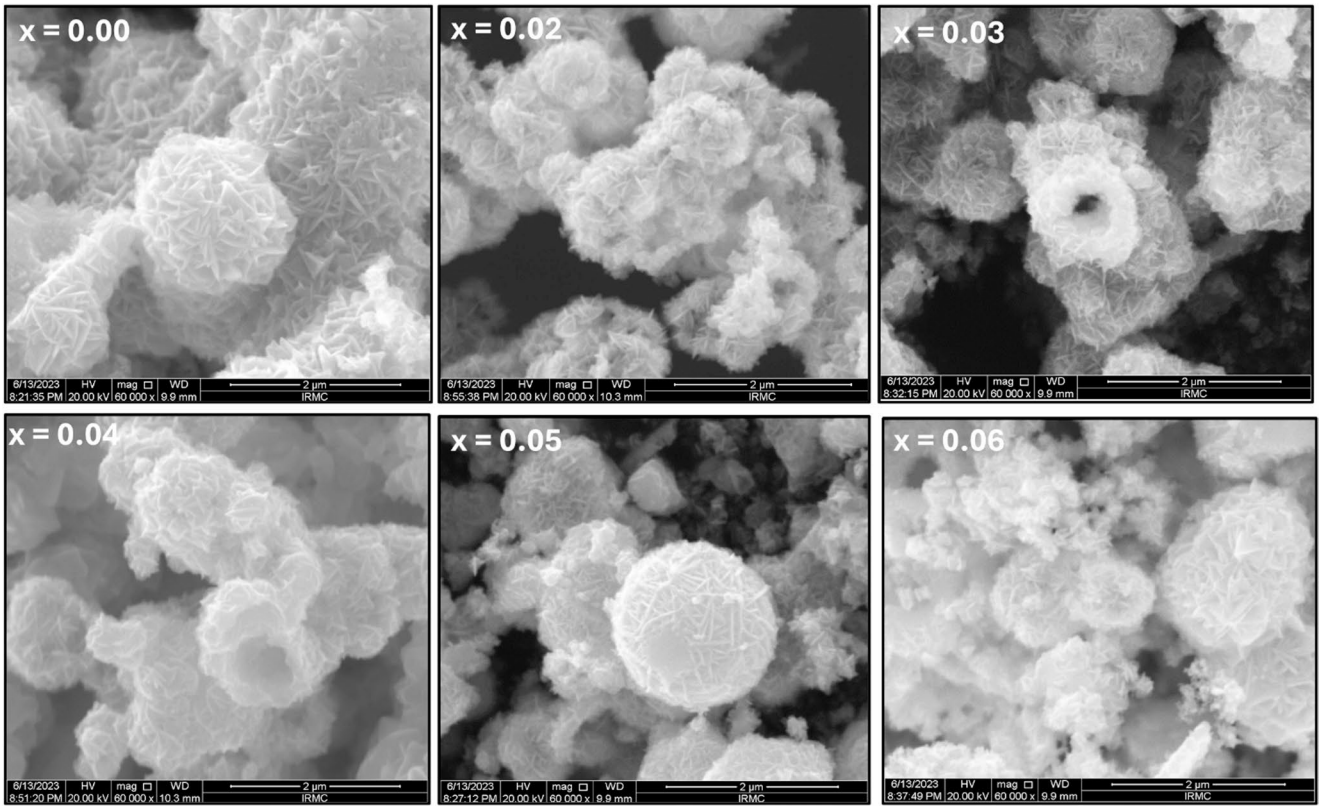

Fig. 3 SEM images of $CoFe_xNi_{2-x}S_4$ ($x \leq 0.06$) NTSs

temperature, and the accompanying magnetic parameters are listed in Table 3. Temperature-dependent *M(H)* variations illustrated in Fig. 7 clearly exhibit the influence of doping within the low field range. At RT, *M(H)* plot of host material ($x = 0.00$) demonstrates that it possesses a diamagnetic nature, which turns into paramagnetic behaviour upon adding Fe^{3+} ions ($x = 0.02$) replacing the Ni^{2+} ions (Fig. 6a). On the other hand, at 10 K, paramagnetic behavior is observed at $x = 0.00$ and 0.02 (Fig. 6b). This paramagnetic behavior is due to the fact that at such a low temperature, the thermal energy is significantly reduced, minimizing the randomizing effects that would otherwise prevent the alignment of magnetic moments. The intrinsic magnetic moments of the individual Co^{2+} and Fe^{3+} ions, which originate from their unpaired electrons, are now more likely to align with the applied external magnetic field. While there is no long-range cooperative ordering between the moments (which would indicate ferromagnetism), their individual alignment with the external field gives rise to the observed paramagnetic behavior. This contrasts with the room temperature behavior where the higher thermal energy prevents this alignment, resulting in a different magnetic state. At both temperatures, hysteresis loops (or ferromagnetic nature) start to show up as soon as Fe doping concentration becomes **x = 0.03** (Figs. 6 and 7).

The diamagnetic behavior exhibited by pure $CoFe_xNi_{2-x}S_4$ ($x \leq 0.06$) NTSs ($x = 0.00$) at RT can be due to the electronic configuration of its ions. Diamagnetism occurs when the material has no unpaired electrons, and the magnetic moments of the electrons in filled shells cancel each other out. On the other hand, at 10 K, thermal energy is reduced, and weak magnetic interactions at RT (high temperature) become more pronounced. In this case, the intrinsic magnetic moments of Co^{2+} and Fe^{3+} ions in host $CoFe_2S_4$ sample are more likely to align with an external magnetic field, revealing paramagnetic behavior. When a small amount of Fe^{3+} ions ($x = 0.02$) are introduced, they replace some of the Fe^{3+} ions in the lattice. Ni^{2+} ions have a different electronic configuration compared to Fe^{3+}, with unpaired electrons that contribute to a net magnetic moment. At this low concentration, the Fe^{3+} ions are too dispersed to interact strongly enough to cause long-range magnetic ordering, resulting in paramagnetism rather than ferromagnetism. At $x = 0.03$, the concentration of Fe^{3+} ions reach a critical level where the interactions between magnetic ions become strong enough to result in long-range magnetic ordering. The increased number of Fe^{3+} ions enhance the superexchange interactions between Ni^{2+} and Fe^{3+} ions, and potentially between Ni^{2+} ions themselves. These interactions can align the magnetic moments of the

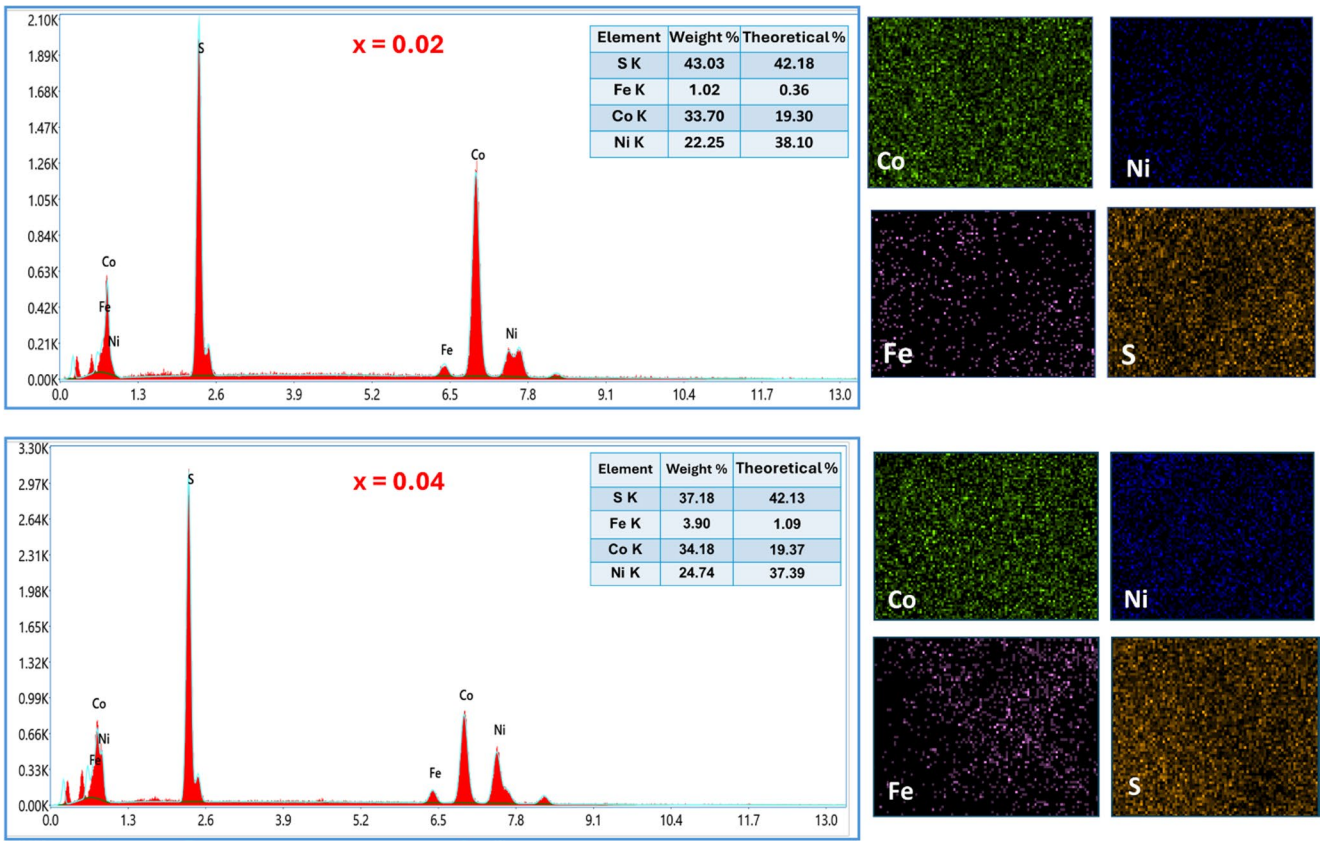

Fig. 4 EDX spectra and elemental mappings of $CoFe_xNi_{2-x}S_4$ (x=0.02 and 0.04) NTSs

ions in a cooperative manner, leading to ferromagnetism and hysteresis loops.

Substituting Ni with Fe introduces magnetic Fe ions into the system, which alters the superexchange interactions between the cations mediated by S anions. A few percent of Fe substitution (2–3%) introduces magnetic ions that disrupt the diamagnetic nature, leading to a paramagnetic state (x=0.02). With slightly higher Fe doping (x=0.03), the system crosses a magnetic percolation threshold (critical concentration for magnetic ordering), establishing long-range ferromagnetic order. This is driven by enhanced cation exchange interactions and site occupancy changes within the spinel structure. The small doping-induced transformation emphasizes the system's sensitivity to Fe content and its potential for tunable magnetism.

The contribution of CoS_2 impurity to the magnetism can depend on its amount and its magnetic interaction with the thiospinels. Ferromagnetic hysteresis loops of $CoFe_xNi_{2-x}S_4$ ($x \leq 0.06$) NTSs appear only after a certain doping concentration (x = 0.03) and are absent at lower concentrations (x = 0.00 and x = 0.02). The presence of CoS_2 as an impurity in all synthesized samples, including the host material (x = 0.00), requires more thorough consideration of its magnetic contribution. CoS_2 is known to be a paramagnetic material above ~ 120 K, but it can display weak ferromagnetism behavior at low temperatures, with a transition close to 120 K [24–26]. At RT, CoS_2 is in its paramagnetic state. For the host sample (x = 0.00), which is intrinsically diamagnetic, the minor paramagnetic contribution from the CoS_2 impurity becomes more noticeable. As Fe doping increases and the sample transitions to a ferromagnetic state, the strong intrinsic ferromagnetism of the $CoFe_xNi_{2-x}S_4$ spinel structure becomes dominant, effectively overshadowing the weaker paramagnetic signal from the impurity. At low temperatures (for instance, 10 K), both the $CoFe_xNi_{2-x}S_4$ samples and the CoS_2 impurity are in magnetically ordered states. The CoS_2 impurity will contribute to the overall magnetic response through its weak ferromagnetic or metamagnetic properties. While its contribution is secondary compared to the primary Fe-doping-induced Ferromagnetism, it could be a factor in the specific shape of the magnetization curves, especially at low doping concentrations where the magnetism of the spinel is still developing. Therefore, while the CoS_2 impurity has an influence, especially at lower temperatures and doping levels, the overall magnetic behavior is primarily driven by the doping-induced changes in the intrinsic magnetic interactions of the $CoFe_xNi_{2-x}S_4$ spinel.

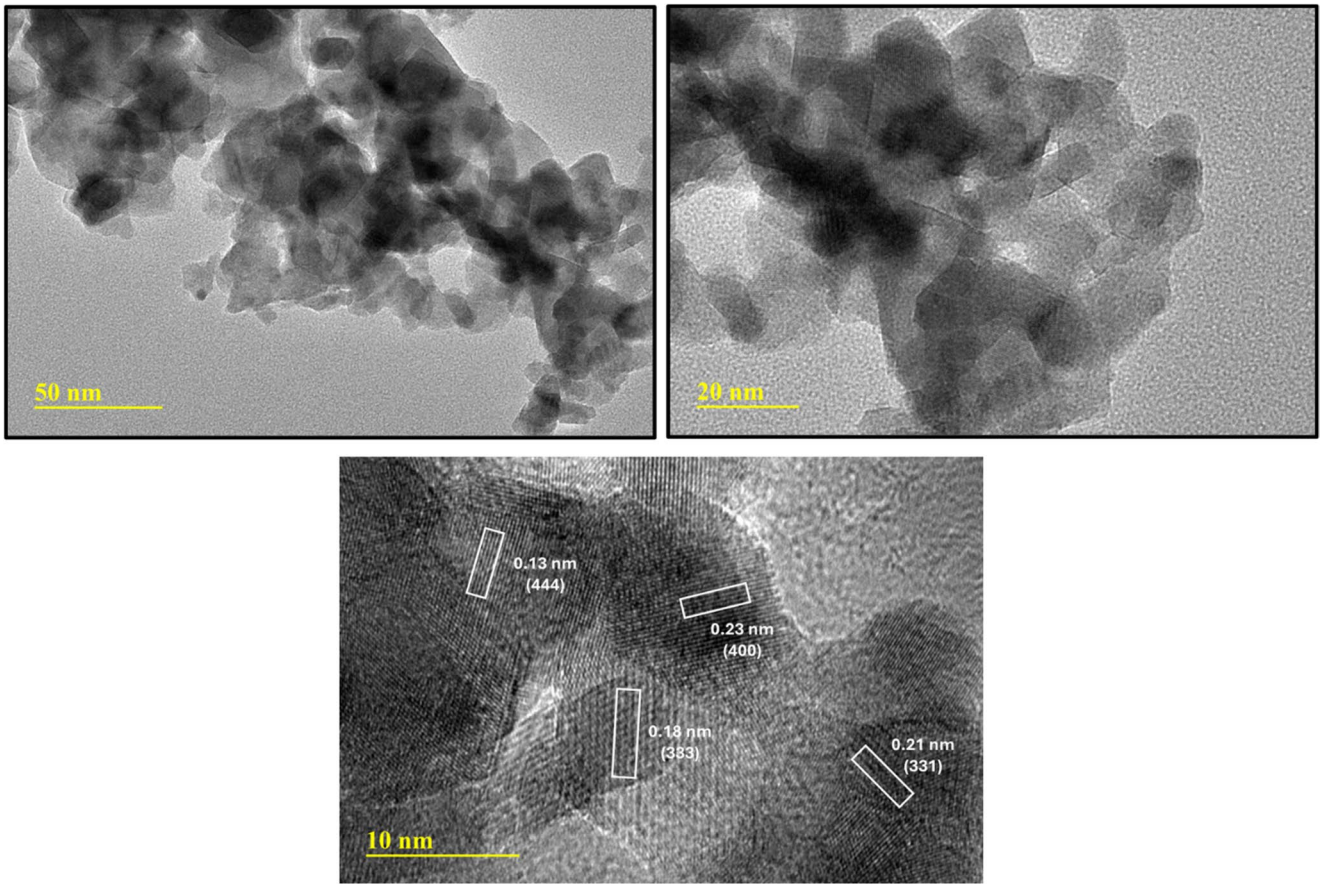

Fig. 5 TEM and HR-TEM images of $CoFe_xNi_{2-x}S_4$ ($x \leq 0.06$) NTSs

Table 2 Cation distribution of $CoFe_xNi_{2-x}S_4$ ($x \leq 0.06$) NTSs

x	A-site [±5%]	B-site [±5%]
0.00	$Co_{0.15}Ni_{0.85}$	$Co_{0.85}Ni_{1.15}$
0.02	$Co_{0.15}Ni_{0.85}$	$Co_{0.85}Fe_{0.02}Ni_{1.13}$
0.03	$Co_{0.15}Ni_{0.85}$	$Co_{0.85}Fe_{0.03}Ni_{1.12}$
0.04	$Co_{0.15}Ni_{0.85}$	$Co_{0.85}Fe_{0.04}Ni_{1.11}$
0.05	$Co_{0.15}Ni_{0.85}$	$Co_{0.85}Fe_{0.05}Ni_{1.10}$
0.06	$Co_{0.15}Ni_{0.85}$	$Co_{0.85}Fe_{0.06}Ni_{1.09}$

At H = 50 kOe, the maximum magnetization (M_{max}) ranges from 0.15 (0.67) emu/g to 2.09 (7.83) emu/g at RT (10 K). The remanence (M_r) values at RT are in the interval from 0.00 to 1.05 emu/g, which is changed to $0.00 \leq M_r \leq 2.01$ emu/g at 10 K. To determine the saturation magnetization (M_s) for $CoFe_xNi_{2-x}S_4$ ($0.03 \leq x \leq 0.06$) NTSs (which are those exhibiting the hysteresis loops) with the help of M vs. $1/H^2$ plots, M is extrapolated to zero at each temperature as depicted in Fig. 8. The estimated M_s values are tabulated in Table 3, which presents that the M_s is within the range of $0.86 \leq M_s \leq 2.09$ ($3.00 \leq M_s \leq 6.81$) at 300 K (10 K). While the M_s reaches its highest magnitude at x = 0.05 at RT, it becomes greatest at x = 0.03 at 10 K. Both the evolution of M_s and M_r with respect to Ni doping ($0.03 \leq x \leq 0.06$) is illustrated in Fig. 9a. The associated magnetic moment (n_B) can be computed employing $n_B = \frac{M_A \times M_s}{5585}$ [27, 28], where M_A stands for the molecular weight. The n_B values for $CoFe_xNi_{2-x}S_4$ ($0.03 \leq x \leq 0.06$) NTSs are found to be very low ($0.05 \leq n_B \leq 0.11$ μ_B) at RT. As the temperature drops to 10 K, they are enhanced ($0.16 \leq n_B \leq 0.36$ μ_B) at each doping content ($0.03 \leq x \leq 0.06$) as expected. In addition to the magnetic moment, the squareness ratio (*SQR*) is another substantial magnetic parameter [27]. The squareness ratio of a magnetic material is defined as the ratio of M_r to M_s, denoted as $SQR=M_r/M_s$. This ratio provides insights into magnetic anisotropy, domain structure, and the ease with which the material can be magnetized and demagnetized. A higher *SQR* (greater than 0.5) typically suggests fewer, larger magnetic domains and stronger magnetic anisotropy [23, 27, 28]. This indicates that a significant portion of the magnetization remains even after the external magnetic field is removed, which is characteristic of materials with strong ferromagnetic interactions. Conversely, a lower SQR value (below 0.5) indicates a multidomain structure where domain walls can move more freely, leading to a significant reduction in remanent magnetization. The squareness ratio is thus a powerful indicator of the magnetic domain state and its evolution with Fe concentration. The *SQR* values of $CoFe_xNi_{2-x}S_4$ ($0.03 \leq x \leq 0.06$) NTSs at each temperature

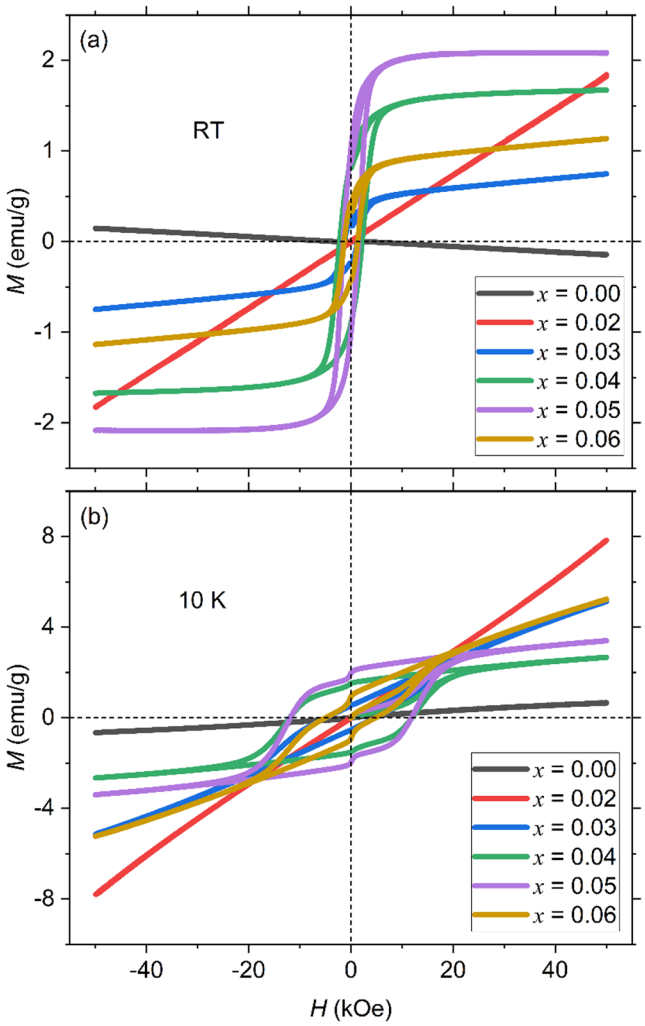

Fig. 6 $M(H)$ curves of $CoFe_xNi_{2-x}S_4$ ($x \leq 0.06$) NTSs at **(a)** RT and **(b)** 10 K

are presented in Table 3. The *SQR* values are around 0.5 for $x = 0.04$ and $x = 0.05$ at both temperatures. It indicates that a significant portion of the magnetization remains when the external magnetic field is removed, suggesting strong ferromagnetic interactions. On the other hand, for $x = 0.03$ and $x = 0.06$, they become approximately 0.3 at RT and 0.1 at 10 K. It suggests larger multidomain structures, where domain walls can move more freely, leading to a reduction in remanent magnetization. At low temperatures, materials often exhibit stronger magnetic anisotropy due to reduced thermal agitation. This anisotropy can cause more complex magnetic domain structures and interactions. The observed kinks in the hysteresis loops at 10 K (Figs. 6b and 7b) are chiefly due to stronger magnetic anisotropy and domain wall pinning. They indicate the presence of multiple magnetic phases or regions with different coercivities and anisotropies. Besides, at low temperatures, enhanced domain wall pinning due to lower thermal energy leads to abrupt changes in magnetization, resulting in kinks. At RT, higher thermal

Table 3 Magnetic parameters of $CoFe_xNi_{2-x}S_4$ ($x \leq 0.06$) NTSs at both RT and 10 K

x	M_{max} (emu/g)		M_s (emu/g)		M_r (emu/g)		SQR		H_c (Oe)		n_B (μ_B)		K_{eff} (erg/g) x10^3		H_a (Oe) x10^3	
	RT	10 K	RT	10 K	RT	10 K	RT	10 K	RT	10 K	RT	10 K	RT	10 K	RT	10 K
0.00	0.15	0.67	-	-	0.00	0.00	-	-	0	0	0.00	0.00	0.0	0.0	-	-
0.02	1.84	7.83	-	-	0.00	0.00	-	-	0	0	0.00	0.00	0.0	0.0	-	-
0.03	0.75	5.14	0.86	6.81	0.26	0.58	0.304	0.085	1341	5098	0.05	0.36	1.79	54.3	4.19	15.9
0.04	1.67	2.66	1.70	3.00	0.91	1.53	0.536	0.509	2254	12,083	0.09	0.16	5.98	56.7	7.04	37.8
0.05	2.09	3.40	2.09	3.80	1.05	2.01	0.502	0.530	1529	11,975	0.11	0.20	4.99	71.0	4.78	37.4
0.06	1.14	5.24	1.24	6.73	0.45	0.98	0.361	0.146	1403	5262	0.07	0.36	2.73	55.3	4.38	16.4

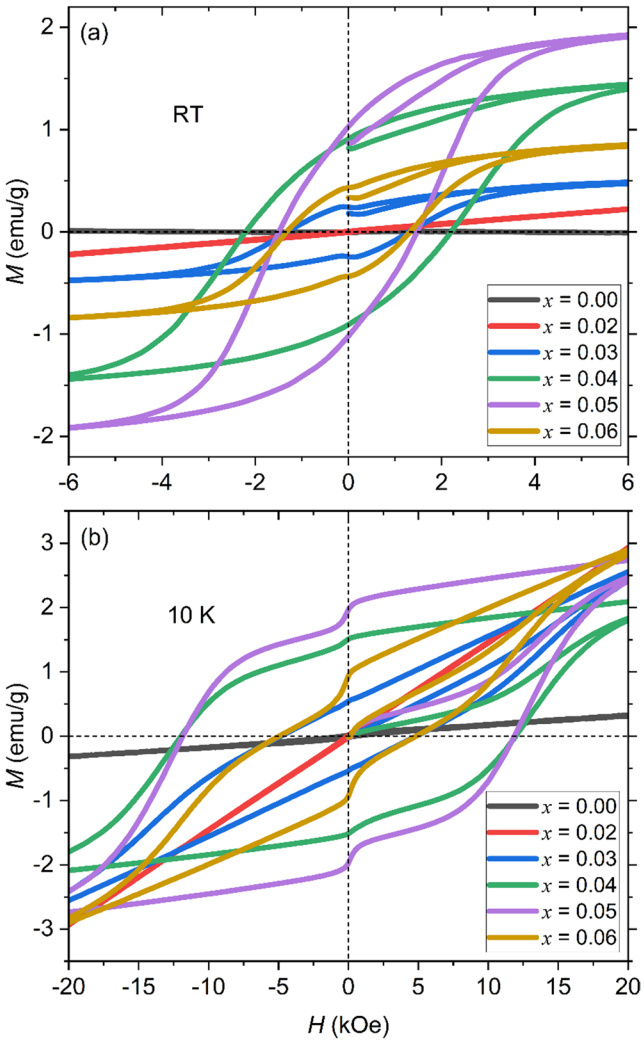

Fig. 7 $M(H)$ curves in an applied field within the low field range for $CoFe_xNi_{2-x}S_4$ ($x \leq 0.06$) NTSs at **(a)** RT and **(b)** 10 K

energy reduces the anisotropy barriers, yielding smoother domain wall movements. This results in smoother hysteresis loops without noticeable kinks, as the magnetization reversal process becomes more continuous and uniform. Additionally, thermal fluctuations at higher temperatures facilitate the alignment of magnetic moments and reduce the distinct steps in the magnetization process, giving rise to smoother hysteresis curves.

The coercivity (H_c) at each Fe doping content is presented in Table 3 which exposes how the H_c improves with increasing *SQR*. The coercivity values of $CoFe_xNi_{2-x}S_4$ ($0.03 \leq x \leq 0.06$) NTSs at both RT and 10 K demonstrate their magnetically hard nature. At 10 K, they are augmented to around 12,000 Oe at x = 0.04 and 0.05. The variation of H_c with Fe concentration is a complex phenomenon influenced by several contributing factors. The coercivity is affected not only by temperature but also several factors such as magneto-crystalline anisotropy and particle size (together with its distribution) [29–35]. The non-linear behavior of H_c can be attributed to the interplay of various anisotropies acting as sources of coercivity, including magneto-crystalline anisotropy, magneto-elastic anisotropy, and surface anisotropy [36]. The substitution of Ni^{2+} with Fe^{3+} induces local lattice strain and alters the spin-orbit coupling, which in turn affects the magneto-crystalline anisotropy and magneto-elastic anisotropy of the material. Furthermore, the observed increase in H_c, particularly at low temperatures, can be related to domain wall pinning at defects, grain boundaries, and the surface of sample. The coercivity is also highly dependent on the crystallite size (D_{XRD}) and porosity of the samples. For example, as the Fe concentration increases, the changes in crystallite size and the potential for increased porosity can create more pinning sites, thereby hinder domain wall motion and increase H_c. These factors collectively contribute to the non-linear changes in coercivity observed in our samples.

The magneto-crystalline anisotropy in the present work is modified upon substituting the Ni^{2+} ions by Fe^{3+} ions, which alters the coercivity accordingly. The associated effective magneto-crystalline anisotropy constant (K_{eff}) is defined as $K_{eff} = \frac{M_s H_c}{0.64}$ [29, 31, 33]. With the help of K_{eff}, the magneto-crystalline anisotropy field (H_a) can be determined through $H_a = \frac{2K_{eff}}{M_s}$ [34] (see Table 3). H_c and H_a are those magnetic parameters characterizing the magnetic phase of nanomaterials. Their evolution with Fe doping ($0.03 \leq x \leq 0.06$) is illustrated in Fig. 9b where, following an initial rise at x = 0.04, they tend to decline. It exhibits the consistent trend between the H_c and H_a with respect to the Ni content. Figure 9a and b show that, at any Fe content, all magnetic parameters (M_s, M_r, H_c, H_a) are augmented with decreasing the temperature due to reduced thermal fluctuations of magnetic moments [35]. Their evolution with respect to Fe doping at each temperature is governed by factors which influence the strength of the exchange interactions. The magnetic properties of spinel ferrites like $CoNiFe_2O_4$ are influenced by the interactions between the metal cations and the anions. In oxides, the superexchange interaction between metal cations through oxygen is a key determinant of magnetic ordering. $CoNiFe_2O_4$ is typically ferrimagnetic, with the magnetic moments of cations on tetrahedral and octahedral sites partially cancelling each other out [37, 38]. Replacing oxygen with sulphur to form $CoNiFe_2S_4$ leads to adjustment in the crystal structure, bond angles and distances between cations and the anion change due to the larger size of S^{2-} compared to O^{2-}. Sulphur's influence on the electronic environment around the cations can lead to different alignments of magnetic moments. It results in accompanying change in magnetic properties due to the different exchange interactions between the metal cations mediated by sulphur (instead of oxygen), influencing the

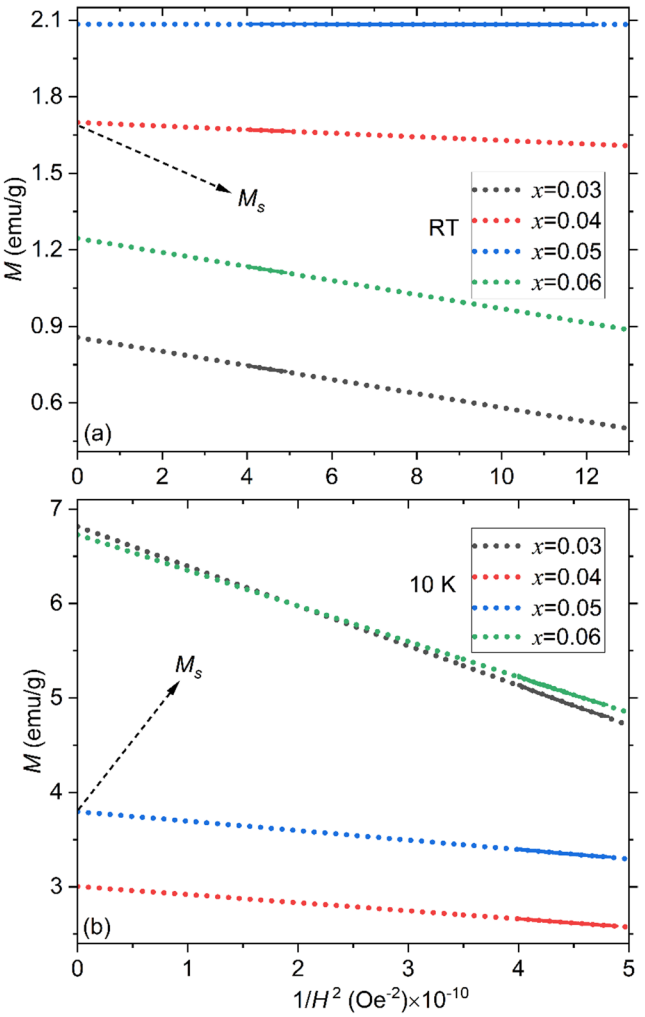

Fig. 8 M vs. $1/H^2$ at **(a)** RT and **(b)** 10 K for $CoFe_xNi_{2-x}S_4$ ($x \leq 0.06$) NTSs

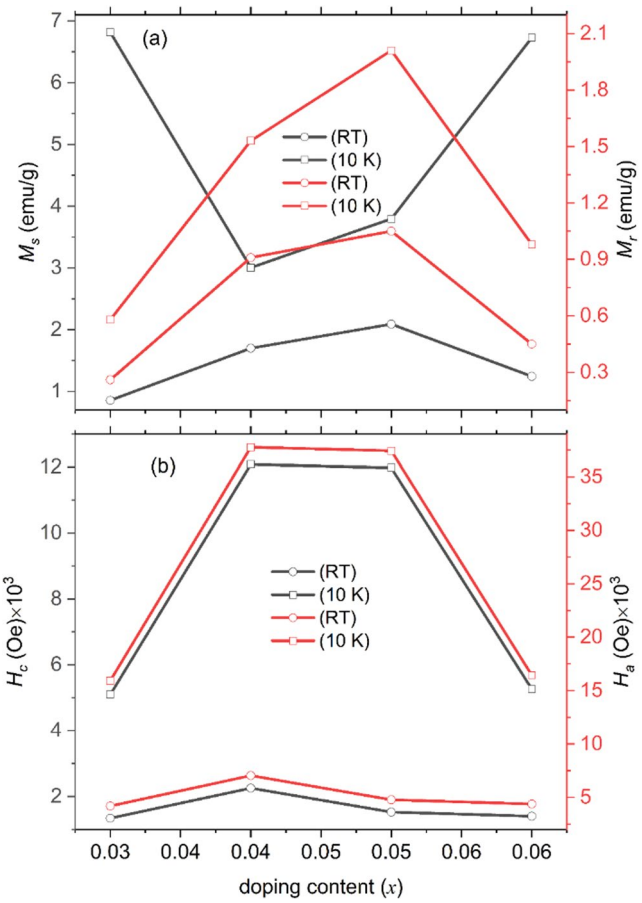

Fig. 9 Magnetic parameters of $CoFe_xNi_{2-x}S_4$ ($x \leq 0.06$) NTSs versus `x` at RT and 10 K

associated magnetic parameters. The effect of Ni dopants on $CuCo_2S_4$ NTSs was reported in an earlier study [39]. In that study, while ferromagnetism was detected for the $CuCo_2S_4$, paramagnetic nature was observed upon addition of Ni atoms at low Ts. It agrees with our findings for $CoFe_xNi_{2-x}S_4$ ($x < 0.03$) NTSs at 10 K. The results in this work highlight that the Fe dopants can be harnessed to achieve desired magnetic properties of $CoFe_xNi_{2-x}S_4$ NTSs.

The non-linear changes of magnetic parameters (M_s, M_r, SQR, etc.) with the concentration of Fe doping are a significant finding and can be explained by several factors. This behavior reflects the competing influences of cation redistribution, surface spin disorder, and interparticle interactions, which collectively govern the effective anisotropy in nanostructured systems. As discussed previously, the system transitions from a paramagnetic to a ferromagnetic state occurred at a critical concentration of $x = 0.03$. This is a non-linear phenomenon. The magnetic properties change abruptly once this threshold is reached. Below this threshold, there is no long-range ferromagnetic order, so parameters like M_s and M_r are effectively zero, while they become non-zero and rapidly increase above the threshold. Furthermore, as reported in our cation distribution analysis, doping Fe^{3+} ions lead to a systematic replacement of Ni^{2+} ions, but this occurs exclusively in the octahedral B-site. The A-site composition remains constant. This specific site preference and the resulting changes in the local environment of the B-site are not linearly proportional to the overall doping concentration, leading to complex and non-linear changes in the magnetic properties. Also, the magnetic properties of these spinel compounds are primarily governed by super-exchange interactions between cations (Ni^{2+}, Fe^{3+}) mediated by the S anions. These interactions are highly sensitive to interatomic distances and bond angles. The systematic introduction of Fe^{3+} into the B-site modifies these super-exchange paths in a non-linear way, as the strength of the interactions depends on the proximity and number of neighboring magnetic ions. Additionally, the presence of CoS_2 impurity and other potential crystal defects can also affect the measured magnetic parameters in a non-linear manner.

These defects can act as pinning sites for domain walls or create localized strain fields that alter magnetic anisotropy. The impact of these defects may be more pronounced at certain doping concentrations, contributing to the observed non-linearity.

3.4 DFT (Density Functional Theory) Calculations

For the sake of completeness, we also conducted DFT calculations on $CoFe_xNi_{2-x}S_4$ NTSs. To that end, pure ($CoNi_2S_4$: CNS) and, using two distinct concentrations, Fe doped ($CoFe_xNi_{2-x}S_4$: FCNS) NTSs are modeled and investigated with the help of QuantumATK software [23, 27, 28]. The influence of Fe dopant on the structural, electronic and magnetic characteristics is demonstrated by formation energy, DOS (spin dependent density of states) and induced spin magnetic moment. Pure CNS composed of 56 atoms: 8 Co, 16 Ni and 32 S atoms. For the doped NTSs, Fe concentrations of x = 1.8% ($FCNS_I$) and x = 3.6% ($FCNS_{II}$) are employed to reveal the effect of doping. The unit cell (with lattice parameters of 9.387 Å) representing the Fe doped NTS is shown in Fig. 10. As Ni has a similar ionic radius to Fe, slight distortions in the lattice occur due to substitution. $FCNS_I$ ($FCNS_{II}$) implies substitution of an (two) Ni atom(s) by a (two) Fe dopant(s) in the unit cell. After modeling them, through setting a force tolerance of 0.01 eV/Å, their optimization is conducted. It yields the optimized individual distances in the unit cell. Next, DFT calculations are implemented using SGGA (spin resolved generalized gradient approximation) with PBE (Perdew-Burke-Ernzerhof) functional (SGGA.PBE) for the electrons' exchange and correlation effects. It was already reported that SGGA can be applied in spinel ferrites [40, 41]. To accurately describe the hybridization of S-*p* and transition metal (TM)-d orbitals, Hubbard (U) correction term is involved in the approximation [41, 42]. It is respectively set to 5.5, 3.3, 3.5 and eV for Ni-*3d*, Co-*3d* and Fe-*3d* electrons. For the ion cores, PseudoDojo pseudopotentials [43] are applied. For the mesh cutoff energy, 120 Hartree with (3,3,3) k-point mesh within the Monkhorst-Pack scheme [44] was employed. The *Medium* basis sets of local numerical orbitals were used to represent the electronic structure of valence electrons.

To the best of our knowledge, for the FCNS NTSs, no theoretical work was reported in the literature. Stability is a crucial factor for potential experimental works and associated applications of nanostructures. The stability of FCNS NTSs is explored with the help of formation energy (FE) which is defined by $FE = (E^t_{system} - \sum_i n_i E^i_{atom}) / \sum_i n_i$ *where* E^t_{system} is the total energy of the system, E^i_{atom} stands for the energy of the isolated atom and n_i denotes the number of individual atoms. The FE is respectively obtained as −1.68, −1.69 and − 1.70 eV for the CNS, $FCNS_I$ and $FCNS_{II}$. They are very close to each other and negative. It indicates that FCNS NTSs are thermodynamically stable, and Fe doping has only a minimal effect on stability. This is consistent with the similar chemical and structural properties of Fe and Ni and suggests that Fe can be incorporated into the CNS without compromising its structural integrity or introducing instability. Thus, Fe doping is energetically favorable and retains stability. In the FCNS NTSs, upon addition of Fe, due to the hybridization between the TM-*d* and S-*p* orbitals, a change in the electronic structure can be expected. It suggests an accompanying coupling between them, which can tune the magnetism. It can be exhibited by the spin magnetic moment per atom with the help of Mulliken analysis [45]. It is respectively obtained as 40.04 μ_B, 42.05 μ_B and 44.05 μ_B for the CNS, $FCNS_I$ and $FCNS_{II}$ structures. As Fe carries a different magnetic moment compared to Ni, the substitution modifies the magnetic ordering due to changes in superexchange interactions between Fe, Co, and the surrounding S atoms. As Fe introduces a higher

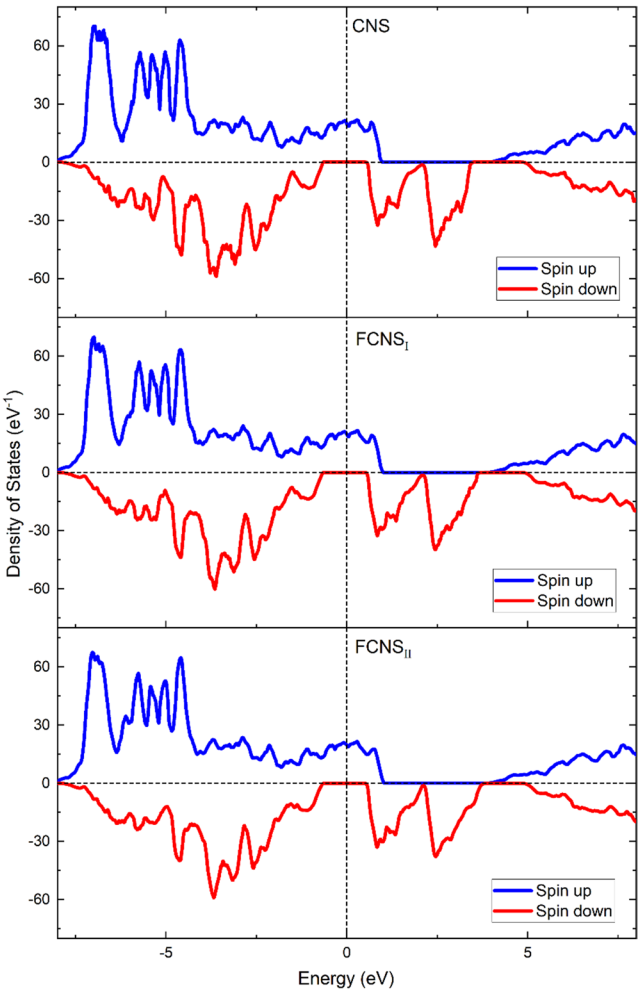

Fig. 10 Spin up and spin down DOS for both pure and Fe doped structures in the energy range $-10\,\text{eV} \leq E \leq 10\,\text{eV}$ in the vicinity of the E_F (which is zero)

magnetic moment than Ni, substituting Ni with Fe enhances the spin magnetic moment of NTSs.

Spin dependent electronic properties are achieved by means of spin up and spin down DOS around the Fermi energy (E_F) as shown in Fig. 10 where E_F is set to zero. A DOS spectrum exhibits the electronic structure of a system and yields data regarding magnetism. The spin dependent DOS shows how the electronic states are distributed for spin up and spin down electrons. For both CNS and FCNS NTSs, the DOS spectra, showing a spin dependent variation for each system, demonstrates a half-metallic behavior as depicted in Fig. 10 where spin up DOS is finite and spin down DOS becomes zero at the E_F. It can be expected due to the strong exchange splitting of the *d*-electrons in TM atoms. Fe doping enhances magnetic interactions, increasing spin polarization and reinforcing half-metallicity. Half-metals exhibit metallic behavior in one spin channel (either spin-up or spin-down) and a band gap in the other. This means that one spin channel is conducting, while the other is insulating, leading to 100% spin polarization at the Fermi level. This property makes materials highly desirable for spintronic applications. An earlier study reported that $CuCo_2S_4$ NTSs could exhibit a metallic property [33]. One can observe metallic characteristics unless corrections, like the Hubbard U term for strong on-site Coulomb interactions, are not incorporated. This term can open a gap as achieved in the present study where spin down energy gap around the E_F is found to be 1.17 eV. The DOS spectra of NTSs show that Fe doping of x = 1.8% and x = 3.6% slightly modify the electronic structure as illustrated in Fig. 10 (where spin dependent DOS is slightly shifted upon introducing the Fe atoms). It can be attributed to the relatively similar electronic configurations of Fe and Ni, the small amount of doping, and the fact that the half-metallic nature of the material is preserved. It suggests that the main effect of Fe doping may be localized and impacts the magnetic properties more than the electronic structure [46–48].

4 Conclusion

This work presented $CoFe_xNi_{2-x}S_4$ ($x \leq 0.06$) NTSs produced by hydrothermally. The XRD showed the formation mixed phases of cubic $CoNi_2S_4$ siegenite and CoS_2. The morphology exhibited three-dimensional woolball particles. M(H) curves of $CoFe_xNi_{2-x}S_4$ ($x \leq 0.06$) NTSs demonstrate that ferromagnetic nature appears when the Fe concentration becomes $x \geq 0.03$. Host sample ($x = 0.00$), while exhibiting a diamagnetic nature at 300 K, possesses a paramagnetic behavior at 10 K. The coercivity values of $CoFe_xNi_{2-x}S_4$ ($0.03 \leq x \leq 0.06$) NTSs at both 300 and 10 K demonstrate their magnetically hard nature. The hysteresis loops, displaying kinks at 10 K, become smoother at 300 K. The squareness ratio becomes around 0.5 at $x = 0.04$ and x = 0.05 at both temperatures, which implies strong ferromagnetic interactions. For samples with $x = 0.03$ and $x = 0.06$, it is found to be approximately 0.3 at 300 K and 0.1 at 10 K. It signifies larger multidomain structures at these Ni concentrations. Replacing oxygen with sulphur to $CoFe_xNi_{2-x}S_4$ leads to adjustment in the crystal structure, bond angles and distances between cations and the anion change due to the larger size of S^{2-} compared to O^{2-}. Sulphur's influence on the electronic environment around the cations can lead to different alignments of magnetic moments. DFT calculation suggested that the main effect of Fe doping may be localized and impacts the magnetic properties more than the electronic structure. Our findings highlight that the Fe dopants can be harnessed to achieve desired magnetic properties of $CoFe_xNi_{2-x}S_4$ NTSs. They might find applications in areas where their unique electrical and magnetic properties are advantageous, such as in certain types of sensors, catalysts, or electronic devices.

Author Contributions S. Caliskan: Data curation, Formal analysis, Investigation, Writing-Original draft preparation. M.A. Almessiere: Conceptualization, Methodology, Resources, Data curation, Writing-Original draft preparation. A. Baykal: Supervision, Conceptualization, Methodology, Investigation, Writing-Reviewing and Editing, Data curation. Y. Slimani: Formal analysis, Investigation, Writing-Reviewing and Editing. A. Mihmanlı : Formal analysis, Investigation. S.E. Shirsath : Formal analysis, Writing-Original draft preparation. L.I. Al-Jumaiah : Investigation.

No Funding was received for this study.

Data Availability Data will be made available on request.

Declarations

Financial Interests The authors declare that they have no known competing financial interests or personal relationships that could have appeared to influence the work reported in this paper.

Competing Interests The authors declare no competing interests.

References

1. Nazar, M., Nasarullah, Aldaghfag, S.A., Yaseen, M., Ishfaq, M., Khera, R.A., Noreen, S., Abdellattif, M.H.: First-principles calculations to investigate structural, magnetic, optical, electronic and thermoelectric properties of X_2MgS_4(X = Gd, Tm) spinel sulfides. J. Phys. Chem. Solids. **166**, 110719 (2022)
2. Song, Y., Sun, D., Jiang, X., Ma, H., Ma, C., Hao, J., Zhang, X.: Enhanced activation of peroxymonosulfate by bimetallic spinel sulfides $CoNi_2S_4$ for organic dye degradation. J. Env. Chem. Eng. **9**, 106889 (2021)
3. Abdpour, S.L., Rademacher, Fetzer, M.N.A., Beglau, T.H.Y., Janiak, C.: Iron-Containing nickel Cobalt Sulfides, Selenides, and

sulfoselenides as active and stable electrocatalysts for the oxygen evolution reaction in an alkaline solution. Solids. **4**, 1810 (2023)
4. Xu, Y.A., Sumboja, Groves, A.T., Ashton, Zong, Y., Darr, J.A.: Enhancing bifunctional catalytic activity of cobalt– nickel sulphide spinel nanocatalysts through transition metal doping and its application in secondary zinc–air batteries. RSC Adv. **10**, 41871 (2020)
5. Xu, S., Zhao, X., Zhang, M., Xu, X., Sun, X., Luo, Z.: Cation substitution for enhanced pseudocapacitance performance of spinel bimetallic sulfides porous nanowires for increased energy storage. Adv. Compos. Hybrid. Mater. **7**, 67 (2024)
6. Gao, Y.P., Huang, K.: $NiCo_2S_4$ Materials for Supercapacitor Applications. Chem. Asian J. **12**, 1969 (2017)
7. Yi, T.F., Pane, J.J., Wei, T.T., Li, Y., Cao, G.: $NiCo_2S_4$-based nanocomposites for energy storage in supercapacitors and batteries. Nano Today **33**, 100894 (2020)
8. Beknalkar, S.A., Teli, A.M., Rendale, S.S., Dhavale, R.P., Bhat, T.S., Shin, J.C., Kim, H.H.: Understanding the supercapacitive properties and charge storage dynamics of $MnCo_2S_4$ bimetallic sulfide electrodes synthesized via a single-step hydrothermal process. Ceram. Int. **50**, 35496 (2024)
9. Liu, S., Wu, J., Wang, X., He, S., Yang, J.: Fabrication of nickel-cobalt sulfide heterostructures with stable thermodynamic interfaces and enhanced electrochemical performance. Chem. Eng. Sci. **293**, 120065 (2024)
10. Li, R., Bai, Z., Hou, W., Qiao, J., Sun, W., Bai, Y., Wang, Z., Sun, K.: Spinel-type bimetal sulfides derived from Prussian blue analogues as efficient polysulfides mediators for lithium-sulfur batteries. Chin. Chem. Lett. **32**, 4063 (2021)
11. Kumar, Y., Govindasamy, M., Pallavolu, M.R., Sambasivam, S., Rao, S.S., Nallapureddy, R.R., Ghfar, A.A., Tighezza, A.M.: Effectively constructed by the interior and interfacecoexisting design of cobalt-doped $NiFe_2S_4$ nanosheets for high-performance supercapacitors. Int. J. Energy Res. **46**, 9358 (2022)
12. Natarajan, S., Duraisamy, V., Subramania, M., Kumar, S.M.S.: Sathya Ponnusamy, effect of Co/Ni ratio on electrocatalytic oxygen evaluation reaction of hydrothermally derived $CoNi_2S_4$ in alkaline medium. Catal. Commun. **184**, 10679 (2023)
13. Cui, X., Yang, X., Liu, Z., Jiang, W., Wan, J., Liu, Y., Ma, F.: Construction of $CoNi_2S_4/Co_9S_8@Co_4S_3$ nanocubes derived from Ni-Co Prussian blue analogues@cobalt carbonate hydroxide core–shell heterostructure for asymmetric supercapacitor. J. Colloid Interface Sci. **661**, 614–628 (2024)
14. Lai, F., Feng, J., Heil, T., Tian, Z., Schmidt, J., Wang, G.-C., Oschatz, M.: Partially delocalized charge in Fe-doped $NiCo_2S_4$ nanosheet–mesoporous carbon-composites for high-voltage supercapacitors. Mater. Chem. A. **7**, 19342 (2019)
15. Khedri, H., Gholizadeh, A.: Experimental comparison of structural, magnetic and elastic properties of $M_{0.3}Cu_{0.2}Zn_{0.5}Fe_2O_4$ (M=Cu, Mn, Fe, Co, Ni, Mg) nanoparticles. Appl. Phys. **125**, 709 (2019)
16. Adineh, Z., Gholizadeh, A.: Comparison of sol–gel and hydrothermal synthesis methods on the physical, and photocatalytic properties of $Bi_{1-x}Ce_xFe_{1-x}Al_xO_3$ ferrites. J. Mater. Sci. : Mater. Electron. **35**, 745 (2024)
17. Biswas, S., Dutta, S., Panja, S.S., Bose, S.: Template-Free Synthesis of "Wool-Ball"-Like Hollow CuS StructuresCan Effectively Suppress Electromagnetic Radiation: A Mechanistic Insight. The Journal of Physical Chemistry C **123**, 17136 (2019)
18. Shao, Z., Zhao, W., Wu, X., Zhu, Q., Wang, C., Han, M., Wu, X.: Anchored effect induced electron-deficient sites in Mo-doped $CoNi_2S_4$ for electrocatalytic oxygen reduction reaction. Mater. Today Chem. **38**, 102119 (2024)
19. Almessiere, M.A., Güner, S., Slimani, Y., Jermy, B.R., Sertkol, Taskhandi, M.N., Korkmaz, A.D., Baykal, A.: Sm-Dy co-substituted Sr hexaferrite microspheres: An investigation on their structural, magnetic, optical, and porosity characteristics. Cer Int. **47**(17), 25131 (2021)
20. Bhoyar, D.N., Somvanshi, S.B., Nalle, P.B., Mande, V.K., Pandit, A.A., Jadhav, K.M.: Multiferroic Fe^{3+} ion doped $BaTiO_3$ Perovskite Nanoceramics: Structural, Optical, Electrical and Dielectric Investigations, J. Phys.: Conference Series 1644 012058. (2020)
21. Slimani, Y., Almessiere, M.A., Shirsath, S.E., Baykal, A., Nawaz, M., Akhtar, S., Ozcelik, B.: Structural, magnetic, optical properties and cation distribution of nanosized $Ni_{0.3}Cu_{0.3}Zn_{0.4}Tm_xFe_{2-x}O_4$ ($0.0 \le x \le 0.10$) spinel ferrites synthesized by ultrasound irradiation. Ultrasonic Sonochemistry. **57**, 203 (2019)
22. Slimani, Y., Almessiere, M.A., Baykal, A., Jermy, R., Auwal, I.A., Shirsath, S.E.: Ce substituted $NiCo_2O_4$ microspheres and nanoflakes: Comparison on magnetic features. Nano-Structures & Nano-Objects **35**, 101000 (2023)
23. Caliskan, S., Almessiere, M.A., Baykal, A., Korkmaz, A.D., Gungunes, Alsalem, H.Z., Slimani, Y., Polat, E.G.: Effects of Pr^{3+} ion doping on magnetic features of Ni–Co nanospinel ferrites synthesized via sonochemical approach. J. Magn. Magn. Mater. **570**, 170492 (2023)
24. Sekiguchi, T., Miyadai, T., Manabe, K.: Ferromagnetic- and paramagnetic resonances in CoS_2 single crystals. J. Magn. Magn. Mater. **28**(1–2), 154–162 (1982)
25. Mushnikov, N.V., Goto, T., Andreev, A.V., Zadvorkin, S.M.: Magnetoelasticity of CoS_2. Philosophical Magazine B **80**(1), 81–93 (2000)
26. Sato, K.: Pyrite type compounds — With particular reference to optical characterization. Progress Cryst. Growth Charact. **11**(3), 109–154 (1985)
27. Akhtar, S., Slimani, Y., Almessiere, M.A., Baykal, A., Polat, E.G., Caliskan, S.: Influence of Tm and Tb co-substitution on structural and magnetic features of $CoFe_2O_4$ nanospinel ferrites. Nano-Structures & Nano-Objects **33**, 100944 (2023)
28. Stoner, E.C., Wohlfarth, E.P.: A mechanism of magnetic hysteresis in heterogeneous alloys. Philosophical Transactions of the Royal Society of London. Series A, Mathematical and Physical Sciences **240**(826), 599–642 (1948)
29. Almessiere, M.A., Baykal, A., Caliskan, S., Slimani, Y., Ul-Hamid, A.: Comparing magnetic characteristics of $CoSe_{3x}Fe_{2-4x}O_4$ ($x \le 0.10$) spinel ferrite nanoparticles synthesized via Sol-Gel and hydrothermal approaches. Nano-Structures Nano-Objects. **38**, 101196 (2024)
30. Caliskan, S., Almessiere, M.A., Baykal, A., Gungunes, H., Slimani, Y., Hassan, M., Klygach, D.S., Kostishin, V.G., Trukhanov, S.V., Trukhanov, A.V., Gondal, M.A.: Impact of vanadium substitution on structural, magnetic, microwave absorption features and hyperfine interactions of SrCo hexaferrites. J. Alloys Compd. **960**, 170578 (2023)
31. Caliskan, S., Almessiere, M.A., Baykal, A., Slimani, Y., Korkmaz, A.D., Gungunes, H., Auwal, I.A.: Structural, magnetic properties, and hyperfine interactions of $Ni_{0.8}Cu_{0.1}Zn_{0.1}Mo_xFe_{2-2x}O_4$ ($0.0 \le x \le 0.1$) nanospinel ferrites. Appl. Phys. A. **129**, 582 (2023)
32. Zhao, L., Yang, H., Cui, Y., Zhao, X., Feng, S.: Study of Preparation and magnetic properties of silica-coated Cobalt ferrite nanocomposites. J. Mater. Sci. **42**, 4110 (2007)
33. Caliskan, S., Almessiere, M.A., Baykal, A., Slimani, Y., Güngüneş, H., Korkmaz, A.D., Ul-Hamid, A., Auwal, I.A.: Magnetic properties of $Sr_{0.5}Ba_{0.5}Ho_xFe_{12-x}O_{19}$ ($x \le 0.10$) nanohexaferrites. Appl. Phys. A. **129**, 616 (2023)
34. Cullity, B.D., Graham, C.D.: Introduction To Magnetic Materials. Wiley, Hoboken, N.J. (2008)
35. Almessiere, M.A., Slimani, Y., Baykal, A., Gungunes, H., Caliskan, S., Vakhitov, M.G., Klygach, D.S., Zubar, T.I., Trukhanov, S.V., Trukhanov, A.V., Ul-Hamid, A.: Impact of Sc^{3+}/In^{3+} ions

co-substitution on structural, magnetic, and microwave features of $SrFe_{12}O_{19}$ hexaferrites. J. Alloys Compd. **968**, 172197 (2023)
36. Mahmoudi, S., Gholizadeh, A.: Effect of non-magnetic ions substitution on the structure and magnetic properties of $Y_{3-x}Sr_xFe_{5-x}Zr_xO_{12}$ nanoparticles. J. Magn. Magn. Mater. **456**, 46–55 (2018)
37. Slimani, Y., Almessiere, M.A., Baykal, A., Gungunes, H., Alsalem, Z., Korkmaz, A.D., Akhtar, S., Caliskan, S.: Impact of Er-Y co-doping on structure, magnetic features, and hyperfine interactions of NiCo nanospinel ferrites: Sonochemical synthesis. Inorg. Chem. Commun. **152**, 110719 (2023)
38. Niu, Z.P., Wang, Y., Li, F.S.: Magnetic properties of nanocrystalline Co–Ni ferrite. J. Mater. Sci. **41**, 5726–5730 (2006)
39. Yue, Z., Hou, Z., Yang, G., Bake, A., Zhao, W., Cortle, D., Hu, C., Cheng, J., Wang, Y.: Observation of itinerant ferromagnetism and coupled magnetoresistance in a spinel $CuCo_2S_4$. J. Mater. Chem. C **9**, 8874 (2021)
40. Fritsch, D., Ederer, C.: First-principles calculation of magnetoelastic coefficients and magnetostriction in the spinel ferrites $CoFe_2O_4$ and $NiFe_2O_4$. Phys. Rev. B **86**, 014406 (2012)
41. Caliskan, S., Rodriguez, A.M., Alexander, S., Almessiere, M.A., Baykal, A., Slimani, Y.: Electronic, magnetic and optical properties of CoNi spinel ferrites doped by rare Earth atoms: A density functional theory study. Discov Mater. **4**, 20 (2024)
42. Caliskan, S., Almessiere, M.A., Baykal, A., Slimani, Y.: A first principles study on electronic structure, magnetic and optical characteristics of Se doped $CoNiFe_2O_4$ spinel ferrites. Computational Materials Science **226**, 112243 (2023)
43. Setten, M., Giantomassi, M., Bousquet, E., Verstraete, M.J., Hamann, D.R., Gonze, X., Rignanese, G.M.: The PseudoDojo: Training and grading a 85 element optimized norm-conserving pseudopotential table. Comput. Phys. Commun. **226**, 39 (2018)
44. Monkhorst, H.J., Pack, J.D.: Special points for Brillouin-Zone integrations. Phys. Rev. B. **13**, 5188 (1976)
45. Soler, J.M., Artacho, E., Gale, J.D., Garcia, A., Junquera, J., Ordejon, P., Sanchez-Portal, D.: The SIESTA method for ab initio order-N materials simulation. J. Phys-Condens. Mat. **14**, 2745 (2002)
46. El Kalai, F., Çınar, E.B., Lai, C.-H., Daoui, S., Chelfi, T., Allali, M., Dege, N., Karrouchi, K., Benchat, N.: Synthesis, spectroscopy, crystal structure, TGA/DTA study, DFT and molecular Docking investigations of (E)-4-(4-methylbenzyl)-6-styrylpyridazin-3(2H)-one. J. Mol. Struct. **1228**, 129435–112943 (2020)
47. Dege, N., Özge, Ö., Avcı, D., Başoğlu, A., Sönmez, F., Yaman, M., Tamer, Ö., Atalay, Y., Kurt, B.Z.: Concentration effects on optical properties, DFT, crystal characterization and α-glucosidase activity studies: Novel Zn (II) complex. Spectrochim. Acta Part A Mol. Biomol. Spectrosc. **262**, 120072 (2021)
48. Sefatgol, R., Gholizadeh, A., Hatefi, H.: Effect of Ti Substitution on the Structural, Optical, and Magnetic Properties of Mn-Mg-Cu-Zn Ferrite Prepared by the Sol–Gel Route. J. Electron. Mater. **53**, 6140–6150 (2024)